Flatband λ-Ti_3O_5 towards extraordinary solar steam generation

https://doi.org/10.1038/s41586-023-06509-3

Received: 16 February 2022

Accepted: 2 August 2023

Published online: 13 September 2023

Check for updates

Bo Yang[1], Zhiming Zhang[1], Peitao Liu[2], Xiankai Fu[1], Jiantao Wang[2], Yu Cao[2], Ruolan Tang[1], Xiran Du[1], Wanqi Chen[1], Song Li[1], Haile Yan[1], Zongbin Li[1], Xiang Zhao[1], Gaowu Qin[1], Xing-Qiu Chen[2] & Liang Zuo[1]✉

Solar steam interfacial evaporation represents a promising strategy for seawater desalination and wastewater purification owing to its environmentally friendly character[1–3]. To improve the solar-to-steam generation, most previous efforts have focused on effectively harvesting solar energy over the full solar spectrum[4–7]. However, the importance of tuning joint densities of states in enhancing solar absorption of photothermal materials is less emphasized. Here we propose a route to greatly elevate joint densities of states by introducing a flat-band electronic structure. Our study reveals that metallic λ-Ti_3O_5 powders show a high solar absorptivity of 96.4% due to Ti–Ti dimer-induced flat bands around the Fermi level. By incorporating them into three-dimensional porous hydrogel-based evaporators with a conical cavity, an unprecedentedly high evaporation rate of roughly 6.09 kilograms per square metre per hour is achieved for 3.5 weight percent saline water under 1 sun of irradiation without salt precipitation. Fundamentally, the Ti–Ti dimers and U-shaped groove structure exposed on the λ-Ti_3O_5 surface facilitate the dissociation of adsorbed water molecules and benefit the interfacial water evaporation in the form of small clusters. The present work highlights the crucial roles of Ti–Ti dimer-induced flat bands in enchaining solar absorption and peculiar U-shaped grooves in promoting water dissociation, offering insights into access to cost-effective solar-to-steam generation.

Along with the world population growth, environmental pollution and climate change, many countries are suffering from a severe shortage of natural freshwater resources. Seawater desalination is obviously an ideal solution to this impending problem[1], as the oceans represent the main water reservoir on Earth. Over the past decade, the solar-driven interfacial water evaporation, capable of localizing solar-generated heat[2,3,8] and hence attaching high-efficiency water distillation, has emerged as a promising and sustainable process to acquire fresh water from seawater or wastewater[2,3,8–14]. Besides, this fundamental process can be extended to electricity generation, steam sterilization, fuel production[5,7] and so on.

To elevate the solar-to-steam generation (SSG) performance, it is essential to increase solar energy absorption, reduce thermal losses, prevent salt blockage and enhance water yield[5]. Towards this goal, exploring high-efficiency and cost-effective photothermal materials is of primary concern. So far, plenty of photothermal materials have been developed, including metallic nanoparticles[4,15], carbon-based materials[16,17], narrow-bandgap semiconductors[6] and hybrid hydrogels[7,11,14,18,19]. By incorporating them into two-dimensional (2D) or three-dimensional (3D) evaporators, a substantial progress on SSG has been achieved[4,6–8,10,14,18–33]. At present, one continuing research effort is dedicated to pursuing more powerful materials for solar energy harvesting.

In principle, the solar absorption ability depends mainly on the characters of photoexcited electron transitions. To access high solar absorptivity, it requires not only a broadband solar absorption, but also sufficiently high joint densities of states (JDOSs). Most previous efforts have focused on using the solar spectrum as broadly as possible[4,6,15,16], whereas the importance of tuning JDOSs in enhancing solar absorption has been less well addressed. Here, the question arises whether one can find a photothermal material that possesses high JDOSs to consolidate ultra-broadband optical transitions for high solar absorption. To meet this purpose, the existence of several flat bands around the Fermi level (E_F) would be a key factor for materials design.

Titanium suboxides (TSOs, Ti_nO_{2n-1}) are featured with abundant oxygen deficiency compared with rutile TiO_2 (refs. 34,35), showing tunable electric, optical and electrochemical properties[6,21]. In contrast to the intrinsic semiconductor TiO_2 absorbing only ultraviolet light, narrow-bandgap semiconductor corundum-Ti_2O_3 (*C*-Ti_2O_3) enables broad solar absorption with a solar absorptivity of 92.5% (ref. 6). Using porous polyvinyl alcohol (PVA) hydrogels mixed with *C*-Ti_2O_3 nanoparticles, Yu et al. reported a record water evaporation rate of 4.0 kg m^{-2} h^{-1} under 1 sun of irradiation[28]. Recently, the metallic λ-Ti_3O_5 nanoparticles have aroused interests due to the existences of photo- or strain-induced reversible λ ↔ β phase transitions[36,37] and external stimulation-controllable heat storage[38,39]. Ohkoshi et al. attributed the λ ↔ β phase transitions to the distortions of Ti–Ti dimers by light-absorbing[36,37] or pressure[38,39]. Some specific valence bands

[1]Key Laboratory for Anisotropy and Texture of Materials (Ministry of Education), School of Materials Science and Engineering, Northeastern University, Shenyang, China. [2]Shenyang National Laboratory for Materials Science, Institute of Metal Research, Chinese Academy of Sciences, Shenyang, China. ✉e-mail: lzuo@mail.neu.edu.cn

related with Ti–Ti dimers were revealed to be central for the optical conductivities of λ- and β-Ti_3O_5 (ref. 37).

In fact, the presence of intrinsic oxygen deficiency in TSOs provides unique chances for the formation of distinct Ti–Ti dimers with diverse electronic band structures. The Ti–Ti dimerization can be identified as a common feature in Ti_nO_{2n-1} for $n > 2$. One would naturally speculate as to whether the wide existence of Ti–Ti dimers in TSOs plays a vital role in promoting solar absorption, and furthermore, whether this feature can be exploited as a pathway to seek desirable photothermal materials through tuning electronic band structures.

To answer these fundamental questions, we performed a combined theoretical and experimental study on Ti_nO_{2n-1} with $n \leq 4$. The metallic λ-Ti_3O_5 powders show the highest mean solar absorptivity of 96.4%. Incorporating them into 3D porous PVA hydrogel evaporators with a conical cavity yields an exceedingly high water evaporation rate of 6.09 ± 0.07 kg m^{-2} h^{-1} under 1 sun of irradiation without salt precipitation. Such an outstanding performance is due to the synergic effects of the peculiar structures occurring in λ-Ti_3O_5, the hierarchical architecture of porous hydrogels and the specific design of conical geometry.

Solar absorptivity of TSOs

The crystal structures of the commercial TiO and *C*-Ti_2O_3 powders were verified by X-ray diffraction, and those of the as-prepared λ-Ti_3O_5, β-Ti_3O_5 and Ti_4O_7 powders were identified using the Rietveld refinements (Supplementary Information 1.1). The morphological feature and hydrophilic property of λ-Ti_3O_5 were revealed (Extended Data Fig. 1 and Supplementary Information 1.2). The optical reflectivity spectra of TiO, *C*-Ti_2O_3, λ-Ti_3O_5, β-Ti_3O_5 and Ti_4O_7 are compiled in Fig. 1a,b. They were predicted by first-principles calculations (Supplementary Information 1.3 and 1.4) and measured by ultraviolet–visible–near-infrared spectroscopy. Both the theoretical and experimental results consistently show that all these TSOs have overall low reflectivities within the full solar spectrum range, where the reflectivities of λ-Ti_3O_5 and β-Ti_3O_5 are much lower than those of the other TSOs. With the measured data, the mean absorptivities in the full solar spectrum range were calculated to be 96.4% for λ-Ti_3O_5 and 95.7% for β-Ti_3O_5, representing the best solar absorptivity among all the considered TSOs.

To capture the underlying mechanism of the overall high solar absorptivity, a detailed analysis of electronic structures was conducted by first-principles calculations. As shown in Fig. 1c,e and Supplementary Information Fig. 1.3, all the considered TSOs are of either metallic state or narrow-bandgap semiconductors. The calculated electronic band structures of λ-Ti_3O_5 and β-Ti_3O_5 are in good agreement with the literature[36,37]. Notably, *C*-Ti_2O_3, λ-Ti_3O_5, β-Ti_3O_5 and Ti_4O_7 share a common feature of relatively flat bands around E_F, originating from the Ti-3*d* states of Ti–Ti dimers (Fig. 1c–g and Supplementary Information 1.5). The existence of such flat bands not only widens the wavelength range of solar absorption, but also creates high JDOSs for effective optical transitions, thus giving rise to overall high solar absorptivity. One can see that the low-lying bands (Ti-a_{1g} states) in *C*-Ti_2O_3 are partially flat in the Brillouin zone (Fig. 1e), whereas the low-lying bands (Ti-d_{xy}-like states with σ bonding) for λ-Ti_3O_5 (Fig. 1c) and β-Ti_3O_5 (Supplementary Information Fig. 1.5) are almost dispersionless in the whole Brillouin zone. This explains why λ-Ti_3O_5 and β-Ti_3O_5 show overall better solar absorptivity than *C*-Ti_2O_3. Further computational tests demonstrate that if the low-lying flat band is removed, the resultant solar absorptivity would be remarkably reduced (Supplementary Information 1.6). These results confirm our idea of enhancing solar absorptivity by tuning electronic band structure, that is, Ti–Ti dimer-induced flat bands with high JDOSs.

For metallic λ-Ti_3O_5, both intraband and interband optical transitions can occur. The intraband optical transitions proceed within the partially filled states near E_F in the near-infrared region, whereas the interband optical transitions come with the transitions from the low-lying flat band to either the (d_{xz}, d_{yz})-like orbitals in the visible region or the ($d_{x^2-y^2}$, d_{z^2})-like orbitals in the ultraviolet region, respectively. All the allowed optical transitions are within the Ti-3*d* orbitals, and they become more pronounced in the visible region as manifested by much larger transition dipole moments (Supplementary Information 1.7). This property is very attractive because the low-lying flat band consolidates optical absorptions in the visible region having high solar spectral irradiance.

Photothermal conversion of TSOs

Various TSO powders were compressed into round pills, and their photothermal conversion capabilities were evaluated using the thermometric method (Supplementary Information 2.1–2.3). When subjected to 1 sun of irradiation, the surface temperatures of the different TSO pills rapidly increased at the initial stages and then approached equilibrium values around 250–500 s. For those pills with thicknesses of roughly 2 mm, the equilibrium temperatures were measured to be 46.6 °C (TiO), 51.5 °C (*C*-Ti_2O_3), 55.7 °C (λ-Ti_3O_5), 55.0 °C (β-Ti_3O_5) and 54.2 °C (Ti_4O_7) (Extended Data Fig. 2), respectively. The λ-Ti_3O_5 pill reached the highest surface temperature (55.7 °C) within the shortest time (roughly 250 s), showing an apparent increase by 4.2 °C with respect to the *C*-Ti_2O_3 pill. It is noted that in the present experimental setup, only a portion of the absorbed solar energy was used to heat the TSO pills and the other was lost by convection, radiation and conduction. The solar-to-heat efficiencies were calculated to be about 70.1% for TiO, 88.2% for *C*-Ti_2O_3, 92.4% for λ-Ti_3O_5, 90.7% for β-Ti_3O_5 and 90.4% for Ti_4O_7 (Supplementary Information Table 2.2). Thus, the metallic λ-Ti_3O_5 provides not only the highest overall solar absorptivity, but also the most effective photothermal conversion among these TSOs.

Indeed, the superior photothermal property of the metallic λ-Ti_3O_5 is intimately related to its specific electronic band structure around E_F. The high JDOSs, resulting from the Ti–Ti dimer-induced flat bands, allow for the creation of high populations of hot electrons and holes by means of photoexcitations. Subsequently, photoexcited hot carriers would continually relax back to the ground state through different relaxation channels. The relaxation dynamics of hot carriers in the near-infrared excitation region is dominated by electron and/or hole–phonon interaction, whereas those in the visible and ultraviolet excitation regions are governed by both electron–electron scattering and electron and/or hole–phonon interaction. During these processes, the absorbed photon energies effectively convert into heat without light emission (Extended Data Fig. 3 and Supplementary Information 2.4). As the high density of states near E_F is expected to have a faster relaxation of photoexcited hot carriers[40], the presence of many flat bands of Ti-3*d* states in λ-Ti_3O_5 certainly facilitates hot carrier relaxation and heat release (Extended Data Fig. 4 and Supplementary Information 2.5). Besides, metallic λ-Ti_3O_5 shows a rather low thermal conductivity (0.20 ± 0.02 W m^{-1} K^{-1})[38], which ensures more solar-generated heat to be localized on its surface layers. In what follows, we shall focus on λ-Ti_3O_5 in light of its superior photothermal conversion performance and low thermal conductivity.

2D SSG

A 2D solar steam evaporator (2D-SSE; Fig. 2a,b) was prepared by dispersing λ-Ti_3O_5 powders (light absorber) onto a cellulose membrane. It was supported by one heat-insulation polyethylene foam sheet (Methods). The water evaporation rates of the 2D-SSE were examined under both dark conditions and 1 sun of irradiation (Supplementary Information 3.1 and 3.2). As a reference, the same measurements were performed on bulk water without the layout of the 2D-SSE.

For the direct evaporation of bulk water, the evaporation rates were measured to be 0.09 kg m^{-2} h^{-1} at an equilibrium temperature (T_E) of 24.8 °C under dark conditions and 0.39 kg m^{-2} h^{-1} at T_E = 29.2 °C

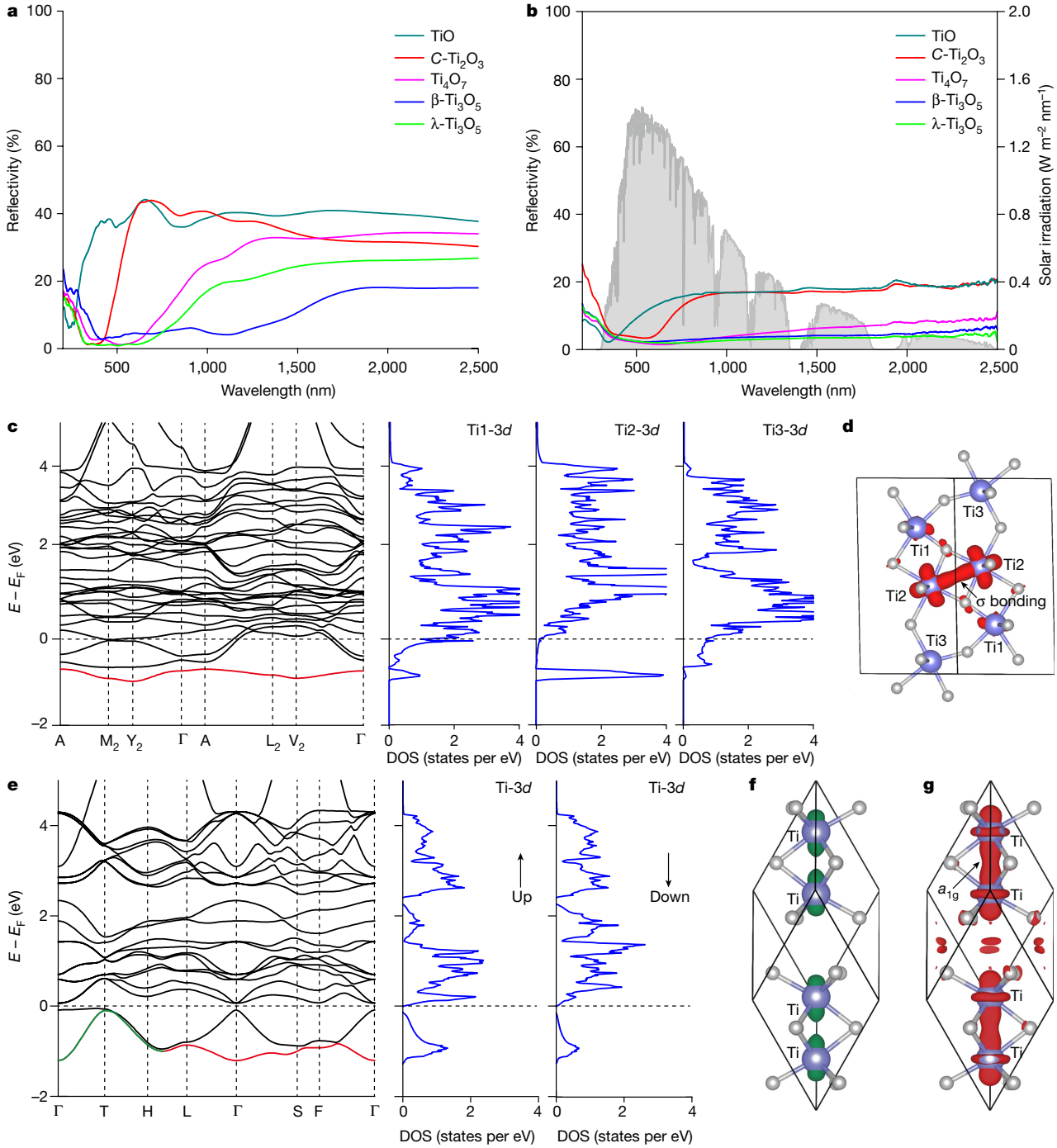

Fig. 1 | Reflectivity spectra and electronic structures. a,**b**, Calculated (**a**) and measured (**b**) reflectivity spectra of TiO, *C*-Ti_2O_3, λ-Ti_3O_5, β-Ti_3O_5 and Ti_4O_7. The grey background in **b** represents the frequency-dependent solar spectrum. **c**, Band structure of λ-Ti_3O_5 and partial densities of states of three types of Ti atom (Ti1, Ti2 and Ti3). **d**, Isosurface of the calculated charge density with an isovalue of 0.1 e Å^{-3} for the low-lying flat band of λ-Ti_3O_5 in **c** to show the charge localization along with the Ti2–Ti2 dimer. **e**, Band structure of *C*-Ti_2O_3 and spin-resolved densities of Ti-3*d* states. **f**,**g**, Isosurfaces of the calculated charge densities with an isovalue of 0.1 e Å^{-3} for the low-lying band of *C*-Ti_2O_3 in **e** to visualize the charge localization around the Ti–Ti dimer. It is noted that the charge localizations in **f** and **g** correspond to the parabolic-like portion along the Γ–T–H path and the nearly flat portion along the H–L–Γ–S–F–Γ path of the low-lying band in **e**, respectively.

under 1 sun of irradiation (Fig. 2c,d), in good agreement with the reported data[6,15]. Using the 2D-SSE, the evaporation rates were measured to be 0.22 kg m^{-2} h^{-1} at T_E = 21.9 °C under dark conditions and 1.64 ± 0.02 kg m^{-2} h^{-1} at T_E = 39.6 °C under 1 sun of irradiation (Fig. 2c,d). The net dark-excluded evaporation rate with the 2D-SSE turns out to be 1.42 kg m^{-2} h^{-1}, which is more than four times that of the bulk water evaporation. This value is close to the theoretical limit (1.47 kg m^{-2} h^{-1})[41] on bulk water under 1 sun of irradiation. The T_E of the 2D-SSE under dark conditions is only 21.9 °C, even lower than the environmental temperature (roughly 25 °C). This anomalous phenomenon should be linked to the interface-assisted evaporation of thin water film adsorbed on the λ-Ti_3O_5 surface.

On the basis of the experimental data, we further estimated the vaporization enthalpy of interfacial water and the efficiency of SSG using the

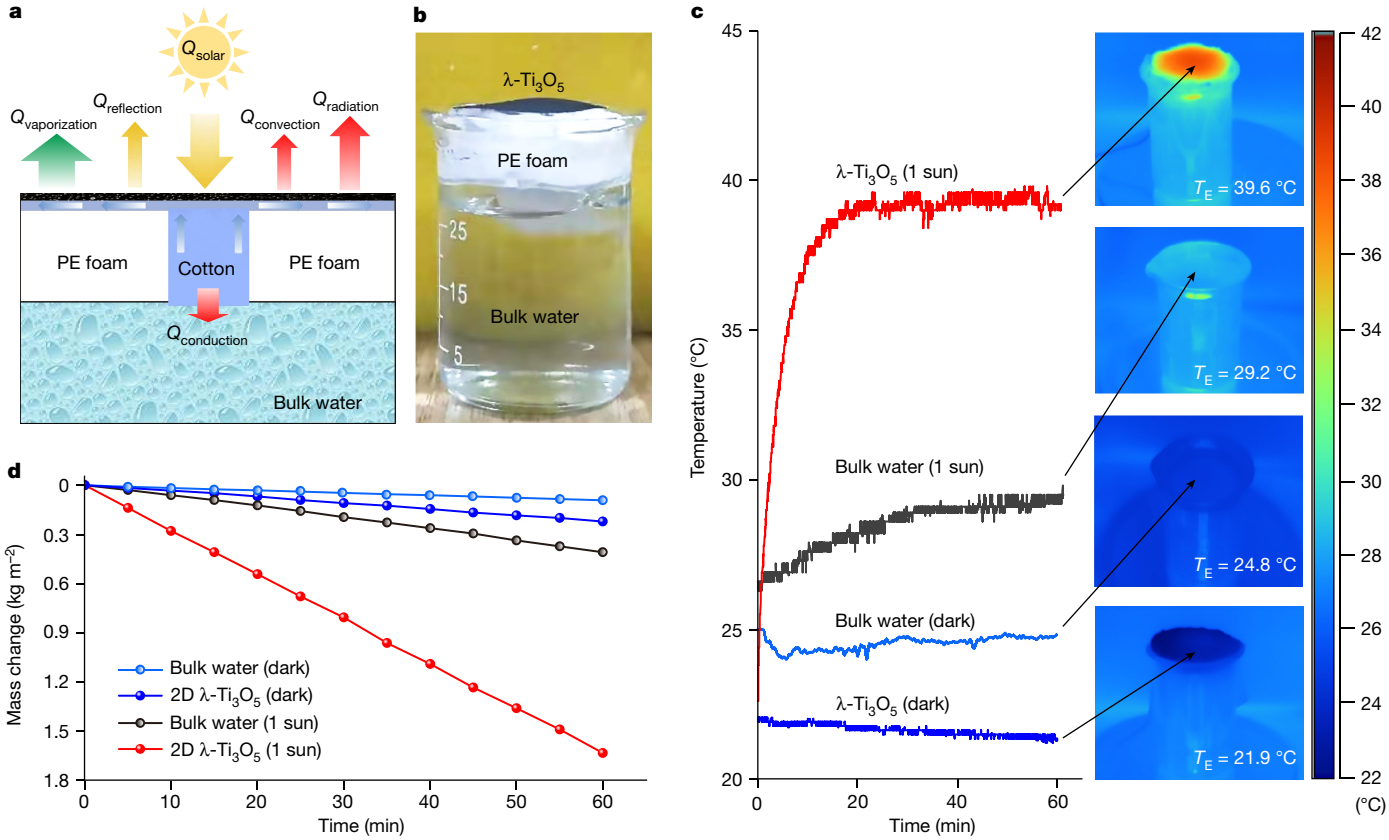

Fig. 2 | 2D-SSE system and experimental results. a, Schematic illustration of the 2D-SSE system. Q_{solar} is the applied sloar energy, $Q_{reflection}$ is the solar energy loss by reflection, $Q_{vaporization}$ is the heat used for water evaporization, $Q_{convection}$ and $Q_{radiation}$ are the convective and radiative thermal losses to the surroundings, respectively, and $Q_{conduction}$ is the conductive thermal loss to bulk water. **b**, Photograph of the 2D-SSE system with light-absorbing λ-Ti_3O_5 powders and heat-insulating polyethylene (PE) foam, floating on bulk water within a 25-ml beaker. **c**, Surface temperatures of the 2D-SSE system and bulk water as a function of time (left) and corresponding infrared photographs (right) on 1 sun of irradiation and dark conditions. **d**, Mass changes of water versus time under 1 sun of irradiation and dark conditions with and without the layout of the 2D-SSE system. All experiments were conducted at the ambient temperature of roughly 25 °C and relative humidity of roughly 40% in an open environment.

thermometric method (Supplementary Information 3.3 and 3.4). Under 1 sun of irradiation, the vaporization enthalpy of water on the surfaces of λ-Ti_3O_5 powders was calculated to be 1,696 kJ kg^{-1} at 39.6 °C, which is about two-thirds of that of bulk water (2,412 kJ kg^{-1} at 40 °C)[41]. The reliability of this value is well supported by our thermodynamic measurements (Supplementary Information 3.5). However, the calculated SSG efficiency is only about 68.30% due to the relatively high surface temperature (39.6 °C) of the 2D-SSE. The solar energy loss by reflection and the thermal losses by convection, radiation and conduction were calculated to be 3.59%, 7.04%, 8.85% and 12.22%, respectively.

To uncover the mechanism for the reduced water vaporization enthalpy, the interactions between interfacial water and λ-Ti_3O_5 surface were investigated by first-principles calculations taking into account the van der Waals interaction. The λ-Ti_3O_5 (1$\bar{1}$0) surface was determined to be the most energetically favourable one (Supplementary Information 4.1). Figure 3a illustrates a clean λ-Ti_3O_5 (1$\bar{1}$0) surface, consisting of two alternative layers within the surface with U-shaped grooves. For the adopted supercell containing six Ti atoms and ten O atoms on each layer (Fig. 3b), all the six surface Ti atoms on the upper layer (forming three Ti–Ti dimers) are fivefold coordinated with O atoms, and the six surface O atoms (O_s) on the upper layer are threefold coordinated with Ti atoms due to one truncated Ti–O bond. The other Ti and O atoms keep the same coordinations as they have in the bulk phase. A peculiar U-shaped groove structure is formed between the upper and lower layers. Once this clean surface is exposed to the air, it will be readily hydrated by chemisorbing water molecules from the air, or hydroxylated[42] by means of dissociating the adsorbed water molecules (Fig. 3c). In this case (Supplementary Information 4.2 and Supplementary Fig. 4.4), the most energetically favourable hydroxylated and hydrated surface refers to three undissociated water molecules (chemisorbed on the Ti sites) and three dissociated water molecules (three OH groups bonded on the Ti sites and three H atoms bonded with the O_s atoms). The presences of the OH and O_sH groups on the Ti sites have been confirmed by attenuated total reflection Fourier transform infrared spectroscopy (Supplementary Information 4.3 and Supplementary Video 1).

The water dissociation only needs to overcome a tiny energy barrier (less than 0.06 eV, Fig. 3f,g), indicating that this process can almost spontaneously occur at finite temperatures. Our long-term (100 ps) ab initio molecular dynamics (AIMD) simulations (Supplementary Information 4.4) have revealed that both water physisorption and dissociation take place with a hydrogen bond linkage to the surface Ti–OH or O_sH groups, when the hydroxylated and hydrated surface is in contact with water (Fig. 3d). An active physisorbed water layer is distinguishable with the frequent occurrence of rapid water dissociation and proton transferring (Supplementary Video 2). This is mainly because above the U-shaped groove, a dissociated H atom tends to bind with its neighbourhood water molecule to form a so-called intermediate H_3O^* unit. Such H_3O^* units are metastable, having a broad lifetime of roughly 2–426 fs (nearly 80% of which lie within 20 fs), as manifested by rapid and frequent exchanges of one of their protons with those of the O_sH groups or a neighbouring water molecule. A detailed Bader charge analysis demonstrates that the fast transfer of H atom between the surface O_sH groups and the H_3O^* units is always

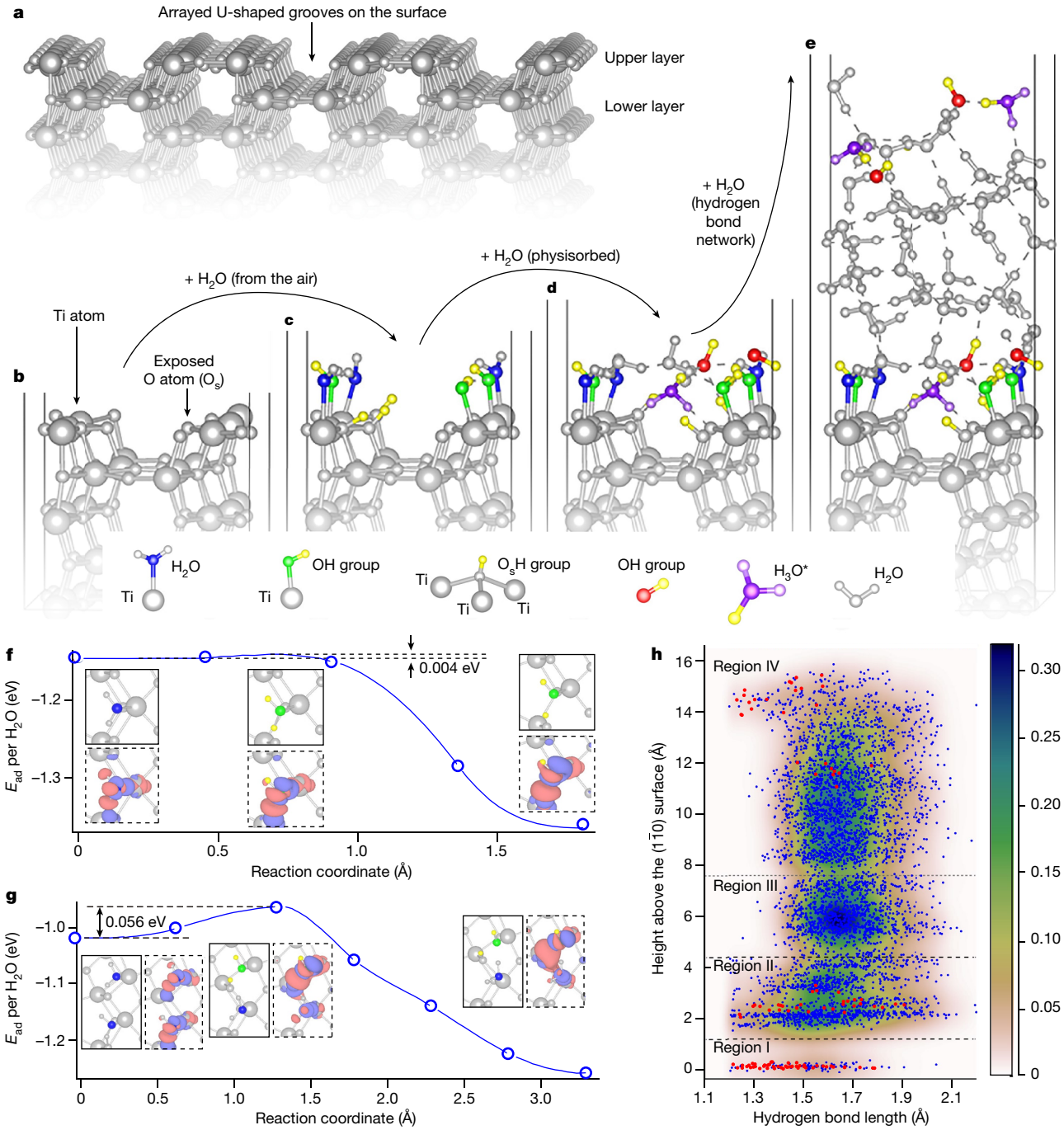

Fig. 3 | Water adsorption and dissociation assisted by the λ-Ti_3O_5 (1$\bar{1}$0) surface. a, Illustration of arrayed U-shaped grooves within the upper and lower layers exposed on the λ-Ti_3O_5 (1$\bar{1}$0) surface. **b**–**e**, Schematics of the clean λ-Ti_3O_5 (1$\bar{1}$0) surface (**b**), the hydroxylated and hydrated λ-Ti_3O_5 (1$\bar{1}$0) surface (**c**), the active physisorbed water layer (**d**) and the hydrogen-bonded network of 49 water molecules (**e**), according to the AIMD simulations. **f**,**g**, Calculated adsorption energy (E_{ad}) per water molecule as a function of the dissociation reaction coordinate when one single water molecule (**f**) and two neighbouring ones (**g**) are adsorbed on the λ-Ti_3O_5 (1$\bar{1}$0) surface. The insets show the local structural details of the initial, transitional and final states, where the isosurfaces of the charge density difference (with an isovalue of ±0.05 e $Å^{-3}$) highlight the charge transfer effect (the pink and blue colours denote electron accumulation and depletion, respectively). **h**, Distributions of selected hydrogen bond lengths along the height above the λ-Ti_3O_5 (1$\bar{1}$0) surface, derived with the AIMD simulations. The red and blue dots denote the hydrogen bonds nearby H_3O^* unit and the other hydrogen bonds of water molecules in regions I, II, III and IV, respectively. The colour bar represents the density of hydrogen bonds.

coupled with charge transfer (Supplementary Information 4.5). This leads to the back-and-forth transfer between H_3O^* and H_2O (Supplementary Video 2), benefiting the evaporation of water in the form of clusters.

Furthermore, our AIMD simulations have captured four distinct water layers above the λ-Ti_3O_5 (1$\bar{1}$0) surface in terms of the density distribution of hydrogen bond length, when increasing the thickness of adsorbed water up to 16 Å (Fig. 3h). Region I contains the hydroxylated and hydrated surface as well as physisorbed water molecules and H_3O^* units above the U-shaped groove, region II corresponds to the active physisorbed water layer, region III is the bulk-like water layer and region IV represents the top water layer next to the vacuum.

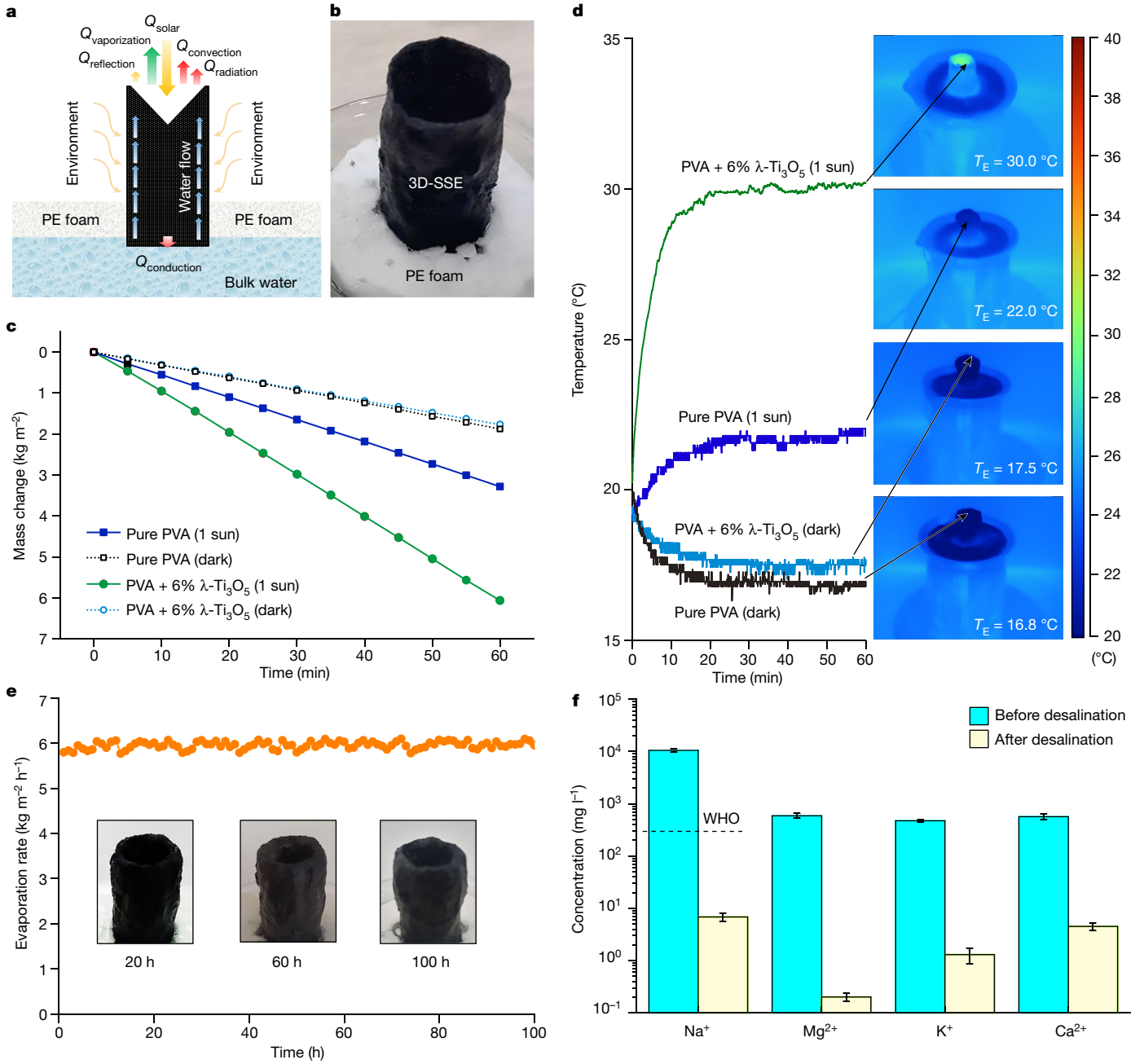

Fig. 4 | 3D solar steam evaporation system and experimental results. **a**,**b**, Schematic illustration (**a**) and the photograph (**b**) of the 3D-SSE system. **c**, Mass changes of water versus time under 1 sun of irradiation and dark conditions for the 3D-SSEs (with and without an addition of 6 wt% λ-Ti_3O_5 powders). **d**, Surface temperatures of the 3D-SSEs (with and without an addition of 6 wt% λ-Ti_3O_5 powders) on 1 sun of irradiation and dark conditions (left) and corresponding infrared photographs (right). **e**, Evaporation rates of 3.5 wt% saline water as a function of time for the 3D-SSE containing 6 wt% λ-Ti_3O_5 powders under 1 sun of irradiation. The insets show the photographs of the 3D-SSE at 20 h, 60 h and 100 h without salt precipitation. **f**, Concentrations of the four main ions (Na^+, Mg^{2+}, K^+ and Ca^{2+}) in the saline water before and after desalination. The error bars of the ion concentrations are the standard deviations of the mean derived with four collected water samples. All experiments were conducted at the ambient temperature of roughly 25 °C and the relative humidity of roughly 40% in an open environment.

The processes of water dissociation, proton transferring and H_3O^* formation frequently occur in both regions II and IV. As long as an H_3O^* unit appears, the lengths of hydrogen bonds surrounding this unit are generally shorter, whereas the lengths of other hydrogen bonds are spread in a wide range, being much wider than those in regions I and III. The shorter hydrogen bonds (roughly 1.2–1.7 Å in Fig. 3h) surrounding the H_3O^* provide the prerequisite for the formation of small clusters of water molecules, whereas the occurrences of the more and longer hydrogen bonds (roughly 1.4–2.2 Å in Fig. 3h) create the necessary condition for the separation of small clusters. Once physisorbed water molecules form small clusters in both regions II and IV, less energy would be required to break hydrogen bonds so that water evaporation becomes easier in the form of small clusters.

It is worth noting that the neutral water clusters $(H_2O)_n$ (n = 3–6) in the gas phase have been identified by infrared spectroscopy[43–46]. Our first-principles calculations further show that when a dissociated H atom is incorporated into one water cluster, the hydrogen bonds between the protonated cluster and its surrounding water molecules

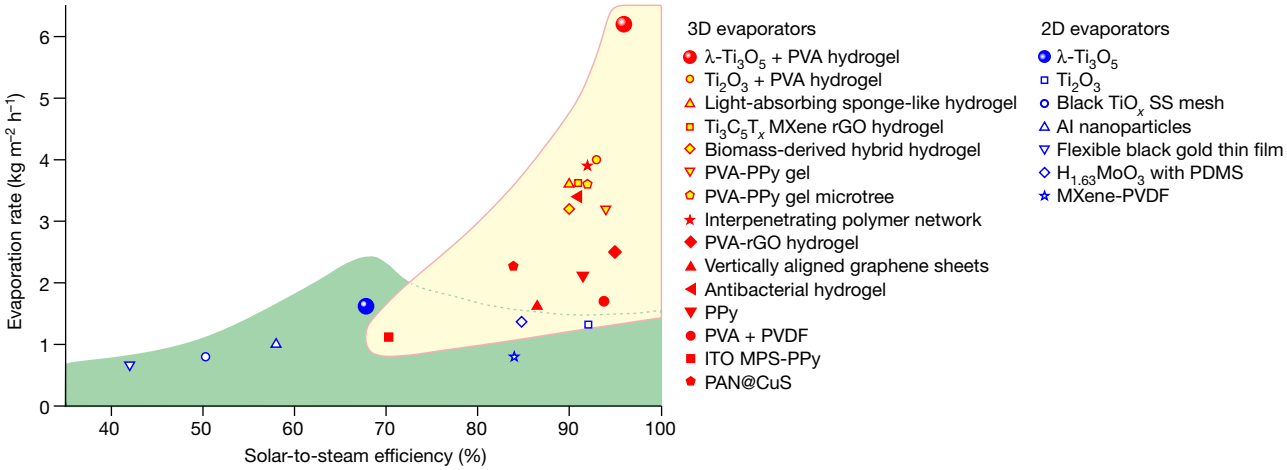

Fig. 5 | Water evaporation rate versus solar-to-steam efficiency for known 2D- and 3D-SSEs under 1 sun of irradiation. Comparisons of our work with the reported results: λ-Ti_3O_5 (this work), Ti_2O_3 (ref. 6), black TiO_x SS mesh[21], Al nanoparticles[4], flexible black gold thin film[24], $H_{1.68}MoO_3$ with polydimethylsiloxane (PDMS)[23] and MXene-PVDF (polyvinylidene difluoride)[20] for 2D-SSEs (marked in blue symbols within the green region), and λ-Ti_3O_5 + PVA hydrogel (this work), Ti_2O_3 + PVA hydrogel[28], light-absorbing sponge-like hydrogel[26], $Ti_3C_2T_x$ MXene rGO hydrogel[25], biomass-derived hybrid hydrogel[27], PVA-PPy gel[14], PVA-PPy gel microtree[11], interpenetrating polymer network[19], PVA-rGO hydrogel[10], vertically aligned graphene sheets[33], antibacterial hydrogel[7], PPy[30], PVA + PVDF[31], ITO MPS-PPy[32] and PAN@CuS (ref. 22) for 3D-SSEs (marked in red symbols within the yellow region). The raw data are given in Supplementary Information Table 6.1.

are weakened (Supplementary Information 4.6). Considering that the Ti–Ti dimers in λ-Ti_3O_5 enable high-efficiency photothermal conversion and the exposed U-shaped grooves promote the formation of small water clusters, we expect that the evaporation of water molecules in the form of clusters[14] would be enhanced. Such a deduction is corroborated by both the Raman spectrum analysis and the measured concentration of Li^+ ions in the evaporated water, which showed that the water molecules tend to evaporate from the λ-Ti_3O_5 surface as small clusters (Extended Data Fig. 5 and Supplementary Information 4.7). This gives an insight into the significant reduction of the water vaporization enthalpy assisted by the surface effects of λ-Ti_3O_5.

3D SSG

To avoid large energy loss with the 2D-SSE, we designed 3D cylindrical evaporators with a conical cavity (3D-SSE; Fig. 4a,b). They were made by mixing λ-Ti_3O_5 powders with porous PVA hydrogel and cotton (Methods), and optimized by adjusting the effective height of 3D-SSE and the weight percentage of λ-Ti_3O_5 powders (Extended Data Fig. 6 and Supplementary Information 5.1 and 5.2). The hierarchical architecture of porous PVA hydrogels and the uniform dispersion of λ-Ti_3O_5 powders greatly enlarge the effective surface area for solar absorption and water evaporation. Moreover, the conical cavity reduces the solar energy loss by reflection and, more importantly, minimizes the heat losses associated with the thermal localization effects.

Our 3D-SSE experiments under 1 sun of irradiation show a water evaporation rate of 3.30 kg m^{-2} h^{-1} for pure PVA, and the highest value of 6.09 kg m^{-2} h^{-1} with an addition of 6 wt% λ-Ti_3O_5 (Fig. 4c). Notably, this record water evaporation rate exceeds those of known 3D evaporators, as shown in Fig. 5 (Supplementary Table 6.1). Under dark conditions, the 3D-SSE with 6 wt% λ-Ti_3O_5 yields a water evaporation rate of 1.78 kg m^{-2} h^{-1}. Under 1 sun of irradiation, the temperature (24.2 °C) of the outer surface of the 3D-SSE is lower than that (30 °C) of the conical cavity surface and even than those (24.5 °C) of the environment and bulk water (Fig. 4d). This means that the surface tension of water on the outer surface of the 3D-SSE should be larger than that on the conical cavity surface, which drives the water-soluble ions to flow from inside to outside. In this way, possible reduction in water evaporation rate caused by salt precipitation can be avoided. Meanwhile, the established temperature gradient of the 3D-SSE guarantees highly efficient use of solar-generated heat for water evaporation. The SSG efficiency of the present 3D-SSE was estimated to be as high as 95.92% on 1 sun of irradiation (Supplementary Information 5.3).

A long-term indoor water desalination experiment was carried out using 3.5 wt% saline water in an open environment. The water evaporation rate of the 3D-SSE remained constant, as high as 5.96 ± 0.08 kg m^{-2} h^{-1} on 1 sun of irradiation for a duration of 100 h, during which no salt precipitation was observed. Both the compression and bending tests show that the present λ-Ti_3O_5 evaporators have excellent mechanical properties and thermal stability (Supplementary Information 5.4). The quality of the desalinated water was measured by inductively coupled plasma spectroscopy. The concentrations of the four main ions (Na^+, Mg^{2+}, K^+ and Ca^{2+}) in the desalinated water were all reduced by about three orders of magnitude, reaching the international standard for drinking water by the World Health Organization (WHO)[47]. Furthermore, the real outdoor water collection experiments were conducted using 3.5 wt% saline water in a closed environment (Extended Data Fig. 7 and Supplementary Information 5.5). The average hourly collection rate was roughly 2.22 kg m^{-2} h^{-1} for a sunny day with a mean solar flux of roughly 78 mW m^{-2} for 10 h, and the average daily yield of purified water was roughly 21.7 l m^{-2} for four sunny days with a mean solar flux of roughly 75.7 mW m^{-2}. This average daily yield of purified water under natural sunlight irradiation for a duration of 10 h is significantly higher than the reported ones[14,18,22,48].

Summary

We demonstrate that the metallic λ-Ti_3O_5 has the highest mean solar absorptivity of 96.4% among the considered TSOs. By incorporating λ-Ti_3O_5 powders into porous PVA hydrogel-based 3D-SSE with a conical cavity, an unprecedentedly high water evaporation rate of 6.09 kg m^{-2} h^{-1} has been achieved under 1 sun of irradiation without salt precipitation. This outstanding performance can be ascribed to three aspects. First, the Ti–Ti dimer induces many flat bands around E_F leading to high JDOSs and hence superior solar absorptivity. This merit of λ-Ti_3O_5, combined with its low thermal conductivity, ensures effective solar-to-heat conversion and high thermal localization. Second, both Ti–Ti dimers and U-shaped grooves exposed on the λ-Ti_3O_5

surface contribute significantly to water adsorption and dissociation. In particular, the frequent appearance of metastable H_3O^* units, accompanied by the fast transferring of protons, facilitates interfacial water evaporation in the form of small clusters. Third, introducing conical cavity enables solar light to go deeper for a better balance between solar evaporation and water supply. Accordingly, the effective surface area for solar absorption and water evaporation is greatly enlarged and capable of preventing salt blockage.

Online content

Any methods, additional references, Nature Portfolio reporting summaries, source data, extended data, supplementary information, acknowledgements, peer review information; details of author contributions and competing interests; and statements of data and code availability are available at https://doi.org/10.1038/s41586-023-06509-3.

1. Elimelech, M. & Phillip, W. A. The future of seawater desalination: energy, technology, and the environment. *Science* **333**, 712–717 (2011).
2. Tao, P. et al. Solar-driven interfacial evaporation. *Nat. Energy* **3**, 1031–1041 (2018).
3. Ni, G. et al. Steam generation under one sun enabled by a floating structure with thermal concentration. *Nat. Energy* **1**, 16126 (2016).
4. Zhou, L. et al. 3D self-assembly of aluminium nanoparticles for plasmon-enhanced solar desalination. *Nat. Photon.* **10**, 393–397 (2016).
5. Zhao, F. et al. Materials for solar-powered water evaporation. *Nat. Rev. Mater.* **5**, 388–401 (2020).
6. Wang, J. et al. High-performance photothermal conversion of narrow-bandgap Ti_2O_3 nanoparticles. *Adv. Mater.* **29**, 201603730 (2017).
7. Guo, Y. et al. Molecular engineering of hydrogels for rapid water disinfection and sustainable solar vapor generation. *Adv. Mater.* **33**, 2102994 (2021).
8. Ghasemi, H. et al. Solar steam generation by heat localization. *Nat. Commun.* **5**, 4449 (2014).
9. Neumann, O. et al. Solar vapor generation enabled by nanoparticles. *ACS Nano* **7**, 42–49 (2013).
10. Zhou, X. et al. A hydrogel-based antifouling solar evaporator for highly efficient water desalination. *Energy Environ. Sci.* **11**, 1985–1992 (2018).
11. Shi, Y., Ilic, O., Atwater, H. A. & Greer, J. R. All-day fresh water harvesting by microstructured hydrogel membranes. *Nat. Commun.* **12**, 2797 (2021).
12. Wu, L. et al. Highly efficient three-dimensional solar evaporator for high salinity desalination by localized crystallization. *Nat. Commun.* **11**, 521 (2020).
13. Zhang, C. L. et al. Designing a next generation solar crystallizer for real seawater brine treatment with zero liquid discharge. *Nat. Commun.* **12**, 998 (2021).
14. Zhao, F. et al. Highly efficient solar vapour generation via hierarchically nanostructured gels. *Nat. Nanotechnol.* **13**, 489–495 (2018).
15. Zhou, L. et al. Self-assembly of highly efficient, broadband plasmonic absorbers for solar steam generation. *Sci. Adv.* **2**, 1501227 (2016).
16. Li, Y. J. et al. 3D-printed, all-in-one evaporator for high-efficiency solar steam generation under 1 sun illumination. *Adv. Mater.* **29**, 1700981 (2017).
17. Zhu, M. W. et al. Plasmonic wood for high-efficiency solar steam generation. *Adv. Energy Mater.* **8**, 201701028 (2018).
18. Guo, Y. H. et al. Tailoring nanoscale surface topography of hydrogel for efficient solar vapor generation. *Nano Lett.* **19**, 2530–2536 (2019).
19. Zhou, X. Y. et al. Topology-controlled hydration of polymer network in hydrogels for solar-driven wastewater treatment. *Adv. Mater.* **32**, 202007012 (2020).
20. Li, R., Zhang, L., Shi, L. & Wang, P. MXene Ti_3C_2: an effective 2D light-to-heat conversion material. *ACS Nano* **11**, 3752–3759 (2017).
21. Ye, M. et al. Synthesis of black TiO_x nanoparticles by Mg reduction of TiO_2 nanocrystals and their application for solar water evaporation. *Adv. Energy Mater.* **7**, 1601811 (2017).
22. Liu, Z. et al. Hierarchical photothermal fabrics with low evaporation enthalpy as heliotropic evaporators for efficient, continuous, salt-free desalination. *ACS Nano* **8**, 13007–13018 (2021).
23. Zhu, Q. et al. A hydrogenated metal oxide with full solar spectrum absorption for highly efficient photothermal water evaporation. *J. Phys. Chem. Lett.* **11**, 2502–2509 (2020).
24. Bae, K. et al. Flexible thin-film black gold membranes with ultrabroadband plasmonic nanofocusing for efficient solar vapour generation. *Nat. Commun.* **6**, 10103 (2015).
25. Lu, Y. et al. Surface patterning of two-dimensional nanostructure-embedded photothermal hydrogels for high-yield solar steam generation. *ACS Nano* **15**, 10366–10376 (2021).
26. Guo, Y. H. et al. Synergistic energy nanoconfinement and water activation in hydrogels for efficient solar water desalination. *ACS Nano* **13**, 7913–7919 (2019).
27. Guo, Y. H. et al. Biomass-derived hybrid hydrogel evaporators for cost-effective solar water purification. *Adv. Mater.* **32**, 1907061 (2020).
28. Guo, Y. H. et al. Tailoring surface wetting states for ultrafast solar-driven water evaporation. *Energy Environ. Sci.* **13**, 2087–2095 (2020).
29. Zhou, X. Y. et al. Architecting highly hydratable polymer networks to tune the water state for solar water purification. *Sci. Adv.* **5**, eaaw5484 (2019).
30. Li, W., Li, Z., Bertelsmann, K. & Fan, D. E. Portable low-pressure solar steaming-collection unisystem with polypyrrole origamis. *Adv. Mater.* **31**, 1900720 (2019).
31. Wang, Y. et al. Improved light-harvesting and thermal management for efficient solar-driven water evaporation using 3D photothermal cones. *J. Mater. Chem. A* **6**, 9874–9881 (2018).
32. Qi, D. P. et al. Polymeric membranes with selective solution-diffusion for intercepting volatile organic compounds during solar-driven water remediation. *Adv. Mater.* **32**, 2004401 (2020).
33. Zhang, P. P. et al. Vertically aligned graphene sheets membrane for highly efficient solar thermal generation of clean water. *ACS Nano* **11**, 5087–5093 (2017).
34. Tominaka, S., Tsujimoto, Y., Matsushita, Y. & Yamaura, K. Synthesis of nanostructured reduced titanium oxide: crystal structure transformation maintaining nanomorphology. *Angew. Chem. Int. Ed.* **50**, 7418–7421 (2011).
35. Huang, S. S. et al. Synthesis of high-performance titanium sub-oxides for electrochemical applications using combination of sol-gel and vacuum-carbothermic processes. *ACS Sustain. Chem. Eng.* **6**, 3162–3168 (2018).
36. Ohkoshi, S. et al. Synthesis of a metal oxide with a room-temperature photoreversible phase transition. *Nat. Chem.* **2**, 539–545 (2010).
37. Mariette, C. et al. Strain wave pathway to semiconductor-to-metal transition revealed by time-resolved X-ray powder diffraction. *Nat. Commun.* **12**, 1239 (2021).
38. Tokoro, H. et al. External stimulation-controllable heat-storage ceramics. *Nat. Commun.* **6**, 7037 (2015).
39. Nakamura, Y., Sakai, Y., Azuma, M. & Ohkoshi, S. Long-term heat-storage ceramics absorbing thermal energy from hot water. *Sci. Adv.* **6**, eaaz5264 (2020).
40. Aeschlimann, M., Bauer, M. & Pawlik, S. Competing nonradiative channels for hot electron induced surface photochemistry. *Chem. Phys.* **205**, 127–141 (1996).
41. Liu, X. et al. Towards highly efficient solar-driven interfacial evaporation for desalination. *J. Mater. Chem. A* **8**, 17907–17937 (2020).
42. Hosseinpour, S. et al. Chemisorbed and physisorbed water at the TiO_2/water interface. *J. Phys. Chem. Lett.* **8**, 2195–2199 (2017).
43. Zhang, B. et al. Infrared spectroscopy of neutral water clusters at finite temperature: evidence for a noncyclic pentamer. *Proc. Natl Acad. Sci. USA* **117**, 15423–15428 (2020).
44. Rognoni, A., Conte, R. & Ceotto, M. How many water molecules are needed to solvate one? *Chem. Sci.* **12**, 2060–2064 (2020).
45. Zwier, T. S. The structure of protonated water clusters. *Science* **304**, 1119–1120 (2004).
46. Miyazaki, M., Fujii, A., Ebata, T. & Mikami, N. Infrared spectroscopic evidence for protonated water clusters forming nanoscale cages. *Science* **304**, 1134–1137 (2004).
47. *Safe Drinking-water from Desalination* (World Health Organization, 2011); http://apps.who.int/iris/bitstream/10665/70621/1/WHO_HSE_WSH_11.03_eng.pdf
48. Yu, Z. et al. Enhanced interfacial solar evaporation through formation of micro-meniscuses and microdroplets to reduce evaporation enthalpy. *Adv. Funct. Mater.* **32**, 2108586 (2022).

Methods

First-principles calculations and AIMD simulations

First-principles calculations were performed using the Vienna ab initio simulation package (VASP)[49–51]. The Perdew–Burke–Ernzerhof method for solids[52] was used for the exchange-correlation functional and the van der Waals interaction was treated by means of the Grimme's D3 method[53]. An effective Hubbard interaction of the Dudarev formulation[54] was imposed on Ti-3*d* orbitals. A plane-wave cutoff of 520 eV was used. The optical properties were calculated by the model Bethe–Salpeter equation method[55,56]. The energy barriers were calculated by the climbing image nudged elastic band method[57]. The charge analysis was performed using the Bader decomposition technique[58]. The transition dipole moments were computed using the VASPKIT code[59]. The AIMD simulations were carried out in NVT ensemble[60,61] with a Nosé–Hoover chain thermostat at 300 K. The velocity Verlet algorithm[62] was adopted to integrate the Newton's equations of motion, and the time step was set to 1 fs. The density of hydrogen bonds against bond length and distance to the surface was evaluated by the kernel density estimation using a Gaussian-type kernel. The smoothing bandwidth was estimated using Scoot's rule[63]. More computational details can be found in Supplementary Information 1 and 5.

Raw materials and preparation of TSO powders

The rutile TiO_2 nanoparticles (25 nm in diameter), titanium monoxide-TiO powders (100 mesh, 99.9% metals basis) and titanium(III) oxide-Ti_2O_3 powders (100 mesh, 99.9% metals basis) were purchased from Aladdin Chemistry Co. Ltd, China. The λ-Ti_3O_5 powders were prepared by sintering the rutile TiO_2 nanoparticles at 1,150 °C for 1 h under a hydrogen atmosphere (flow rate of 1.5 l min^{-1}), followed by a slow cooling process (3 K min^{-1}) from the sintering temperature to room temperature. The Ti_4O_7 powders were prepared using the same fabrication method as the λ-Ti_3O_5 powders but under a small flow rate of hydrogen (0.75 l min^{-1}). The β-Ti_3O_5 powders were prepared from the λ-Ti_3O_5 powders by applying a stress of 1,500 MPa.

Characterizations of crystal structure, morphology, reflectivity and photoluminescence

The crystal structures of the TSO powders were examined using a Rigaku SmartLab X-ray diffractometer with Cu-K*α* radiation (1.54056 Å in wavelength) at a voltage of 40 kV and a current of 200 mA with a scan step of 0.04°. The morphologies of all samples were observed with a field-emission scanning electron microscope (SEM, JEOL JEM7001F) operated at 15 kV and a transmission electron microscope (TEM, JEOL 2100 F) operated at 200 kV. The diffuse reflectance spectra of the TSO powders were measured by an ultraviolet–visible–near-infrared spectrometer (Shimadzu UV-3600 Plus) attached to an integrating sphere (ISR-3100). All infrared photographs were taken using a Fluke Ti400 infrared thermal camera. The photoluminescence effect of λ-Ti_3O_5 powders was examined using the FLS1000 photoluminescence spectrometer.

Identification of water adsorption on λ-Ti_3O_5 surface

Attenuated total reflection Fourier transform infrared spectroscopy (Thermo Scientific, Nicolet iS10) was used to explain the status of water adsorption on the surfaces of λ-Ti_3O_5 particles. The predried λ-Ti_3O_5 powders were first spread on a germanium crystal, and then wetted with a few drops of water, followed by an immediate irradiation under simulated solar light. The in situ attenuated total reflection Fourier transform infrared spectroscopy measurements were conducted at room temperature every 2 min, within the wavenumber range from 400 to 4,000 cm^{-1}.

Fabrication of 2D evaporator

The λ-Ti_3O_5 powders with a weight of roughly 10 mg were dispersed well in 10 ml of deionized water, under the assistance of an ultrasonic bath. To prepare a 2D evaporator, the dispersed mixture was deposited on a cellulose membrane (30 mm in diameter and roughly 100 μm in thickness) through vacuum suction filtration. The deposited cellulose membrane was then put on the top of one circular polyethylene foam sheet as the heat insulator to bulk water. Before this, the polyethylene foam sheet was pierced with a hole in the middle (10 mm in diameter) and a cotton core was filled in the hole for water transportation. The integrated 2D evaporator system was floating on bulk water within a beaker (25 ml) for the water evaporation measurements.

Fabrication of 3D evaporator

Two kinds of PVA, with molecular weights of 13,000–23,000 and 27,000, were mixed in a ratio of 5/7. To prepare hydrogels, 1.05 g of the mixed PVA were dissolved into 15 ml of water at 70 °C and stirred for 30 min as the solution A. Then, 2 ml of glutaraldehyde solution and 0.15 g $NaHCO_3$ powders were added into the solution A as the solution B. The λ-Ti_3O_5 powders with a given mass fraction (from 2 to 10 wt%) and roughly 2 mg of cotton fibres were mixed into the solution B. The mixtures were put into a 3D module and, subsequently, 10 ml of HCl (3 wt%) were added to make them porous. The prepared porous hydrogels were immersed in deionized water overnight to remove non-reacted chemicals, followed by freeze–drying three times at −20 °C for 8 h. After the freeze–drying process, the porous hydrogels were cut into individual cylindrical 3D evaporators (15 mm in diameter) of different heights, with or without a conical cavity (14 mm in diameter and 6 mm deep) on the top.

Characterization of solar evaporation performance

The evaporation performances of the 2D- and 3D-SSE systems were measured under 1 sun of irradiation (AM1.5G, 1,000 W m^{-2}). A Xenon lamp (Solar-300, China Education Au-light Co., Ltd) was selected as the simulated solar source, in which the intensity of light was calibrated using a photodiode. In the experiments, an aperture was attached to tightly control the amount of light incident on the light absorbers[64]. Each integrated evaporator system was put in a 25-ml (or 50-ml) beaker and subjected to the simulated solar irradiation. The mass change of the beaker was recorded in real time using an electronic balance, in which the reduced mass was counted as the quantity of evaporated water. For the SSG test, the room temperature was around 25 °C and the relative humidity was roughly 40% in an open environment. The evaporation rate under dark conditions was also measured and used to calibrate the SSG data. Both the Raman spectral analysis[65] and the Li^+ ion concentration tracing method[14] were adopted to prove the enhanced formation of water clusters by λ-Ti_3O_5. The vaporization enthalpies of water were determined using the thermometric method[3] as well as differential scanning calorimetry (TA Instruments, DSC25).

Characterization of seawater desalination performance

To prove the long-term seawater desalination stability of the 3D-SSE, an experiment was carried out using 3.5 wt% saline water under 1 sun of irradiation, consecutively tested for 100 h. To check whether or not salt precipitation occurs during the desalination process, the surface condition of the 3D-SSE was monitored. The mass change was recorded every hour, and the evaporative flux was derived accordingly. The quality of product water was evaluated by inductively coupled plasma-mass spectrometry. The indoor water collection experiments were conducted under the simulated sunlight irradiation. A group of 16 cylindrical evaporators were evenly inserted into the foamed polyethylene sheet (8 mm in thickness), floating on the 3.5 wt% saline water in a container. The outdoor solar desalination experiments were performed using the cylinder-shaped 3D-SSEs with a conical cavity under natural sunlight irradiation on the campus of Northeastern University, Shenyang, China. A group of 63 3D-SSEs were inserted

into the foamed polyethylene, floating on the 3.5 wt% saline water in a container. The intensities of the natural sunlight shined on the roof (made of transparent quartz glass) of the evaporation device and the yields of the accumulated clean water were carefully traced during the day time from 07:30 to 17:30. The detailed experimental conditions are given in Supplementary Information 5.5.

Data availability

Raw data that support the plots in this paper and other findings in the paper and the Supplementary Information are available from the corresponding author on request. Source data are provided with this paper.

Code availability

VASP is a source suite of computational tools available at www.vasp.at. The other codes written for use in this study are available from the corresponding author upon reasonable request.

49. Kresse, G. & Hafner, J. Ab initio molecular dynamics for liquid metals. *Phys. Rev. B* **47**, 558–561 (1993).
50. Kresse, G. & Furthmüller, J. Efficient iterative schemes for ab initio total-energy calculations using a plane-wave basis set. *Phys. Rev. B* **54**, 11169–11186 (1996).
51. Kresse, G. & Joubert, D. From ultrasoft pseudopotentials to the projector augmented-wave method. *Phys. Rev. B* **59**, 1758–1775 (1999).
52. Perdew, J. P. et al. Restoring the density-gradient expansion for exchange in solids and surfaces. *Phys. Rev. Lett.* **100**, 136406 (2008).
53. Grimme, S., Antony, J., Ehrlich, S. & Krieg, H. A consistent and accurate ab initio parametrization of density functional dispersion correction (DFT-D) for the 94 elements H–Pu. *J. Chem. Phys.* **132**, 154104 (2010).
54. Dudarev, S. L. et al. Electron-energy-loss spectra and the structural stability of nickel oxide: an LSDA+U study. *Phys. Rev. B* **57**, 1505–1509 (1998).
55. Bokdam, M. et al. Role of polar phonons in the photo excited state of metal halide perovskites. *Sci Rep.* **6**, 28618 (2016).
56. Liu, P. et al. Relativistic GW+BSE study of the optical properties of Ruddlesden–Popper iridates. *Phys. Rev. Mater.* **2**, 075003 (2018).
57. Henkelman, G., Uberuaga, B. P. & Jónsson, H. A climbing image nudged elastic band method for finding saddle points and minimum energy paths. *J. Chem. Phys.* **113**, 9901–9904 (2000).
58. Henkelman, G., Arnaldsson, A. & Jónsson, H. A fast and robust algorithm for Bader decomposition of charge density. *Comput. Mater. Sci.* **36**, 354–360 (2006).
59. Wang, V. et al. VASPKIT: a user-friendly interface facilitating high-throughput computing and analysis using VASP code. *Comput. Phys. Commun.* **267**, 108033 (2021).
60. Nosé, S. A unified formulation of the constant temperature molecular dynamics methods. *J. Chem. Phys.* **81**, 511–519 (1984).
61. Hoover, W. G. Canonical dynamics: equilibrium phase-space distributions. *Phys. Rev. A* **31**, 1695–1697 (1985).
62. Verlet, L. Computer 'experiments' on classical fluids. I. Thermodynamical properties of Lennard-Jones molecules. *Phys. Rev.* **159**, 98–103 (1967).
63. Scott, D. W. *Multivariate Density Estimation: Theory, Practice, and Visualization* (John Wiley & Sons, 1992).
64. Li, X. Q. et al. Measuring conversion efficiency of solar vapor generation. *Joule* **3**, 1798–1803 (2019).
65. Chen, X. et al. Highly efficient photothermal conversion and water transport during solar evaporation enabled by amorphous hollow multishelled nanocomposites. *Adv. Mater.* **34**, 2107400 (2022).

Acknowledgements We are grateful to N. Wang and H. L. Qu at Analytical and Testing Center, Northeastern University, for the photoluminescence measurements and to Y. N. Jiang at Analytical and Testing Center, Institute of Metal Research, Chinese Academy of Sciences for the thermal conductivity measurements. This work was supported by the Program of Introducing Talents of Discipline Innovation to Universities 2.0 (grant no. BP0719037), China.

Author contributions B.Y., S.L., X.-Q.C., G.Q. and L.Z. conceived the idea and designed the experiments. Z.Z., R.T. and W.C. performed most of the experiments. P.L., J.W., Y.C., X.F. and H.Y. performed the first-principles calculations. Z.L., X.Z. and X.D. provided some help with the data analysis. B.Y., X.-Q.C., P.L. and L.Z. co-wrote the paper. All authors discussed the results, revised and approved the paper.

Competing interests The authors declare no competing interests.

Additional information

Supplementary information The online version contains supplementary material available at https://doi.org/10.1038/s41586-023-06509-3.

Correspondence and requests for materials should be addressed to Liang Zuo.

Peer review information *Nature* thanks Xianbao Wang and the other, anonymous, reviewer(s) for their contribution to the peer review of this work.

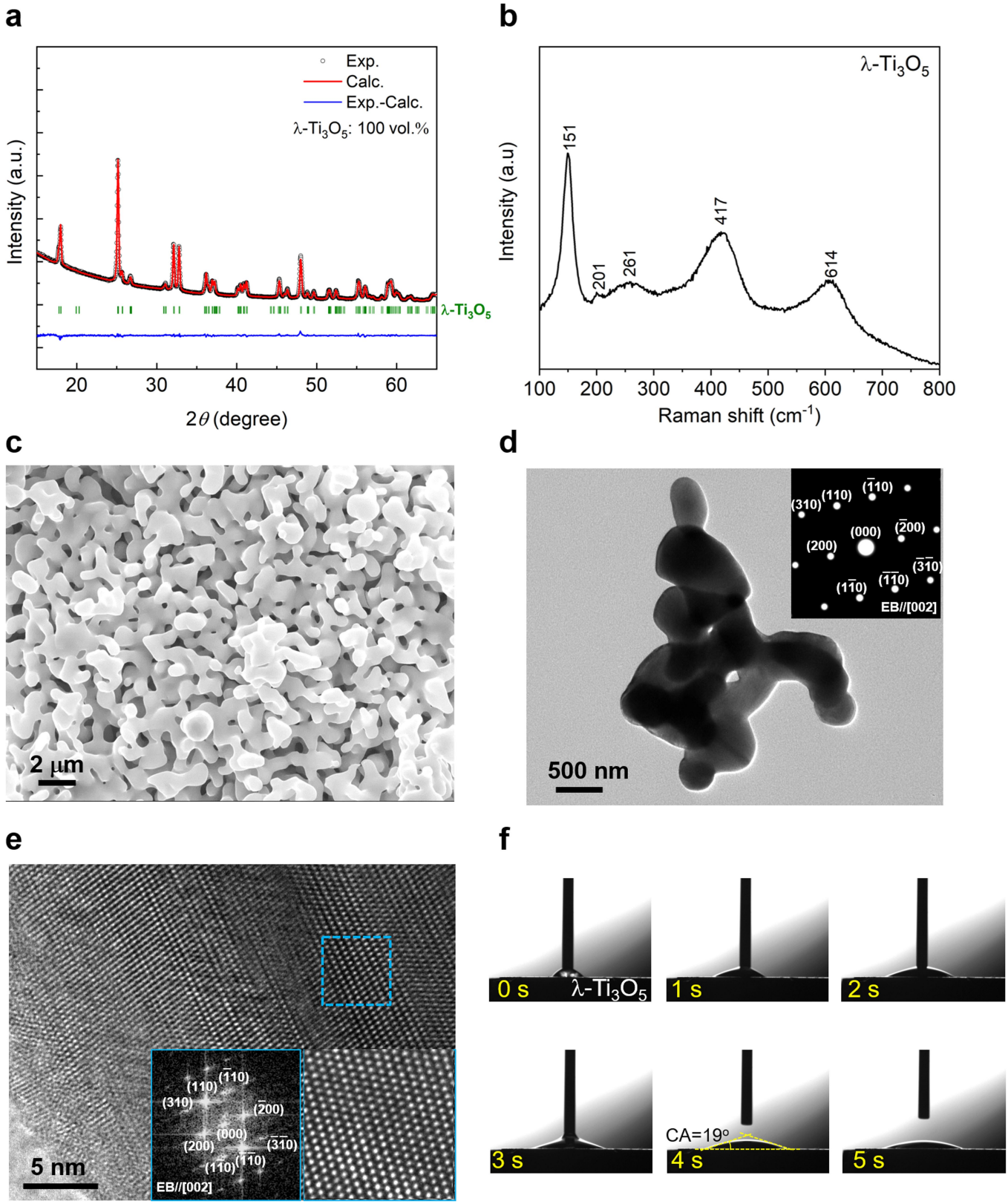

Extended Data Fig. 1 | Structural and morphological characterization, and hydrophilicity test of λ-Ti_3O_5. a, Rietveld refinement of the experimental XRD pattern. **b**, Raman spectrum. **c**, SEM image. **d**, TEM bright-field image. **e**, High-resolution TEM image (Inset: the Fast-Fourier transformation of the dotted blue area). **f**, Contact angle test. More details are given in Supplementary Information 1.1 and 1.2.

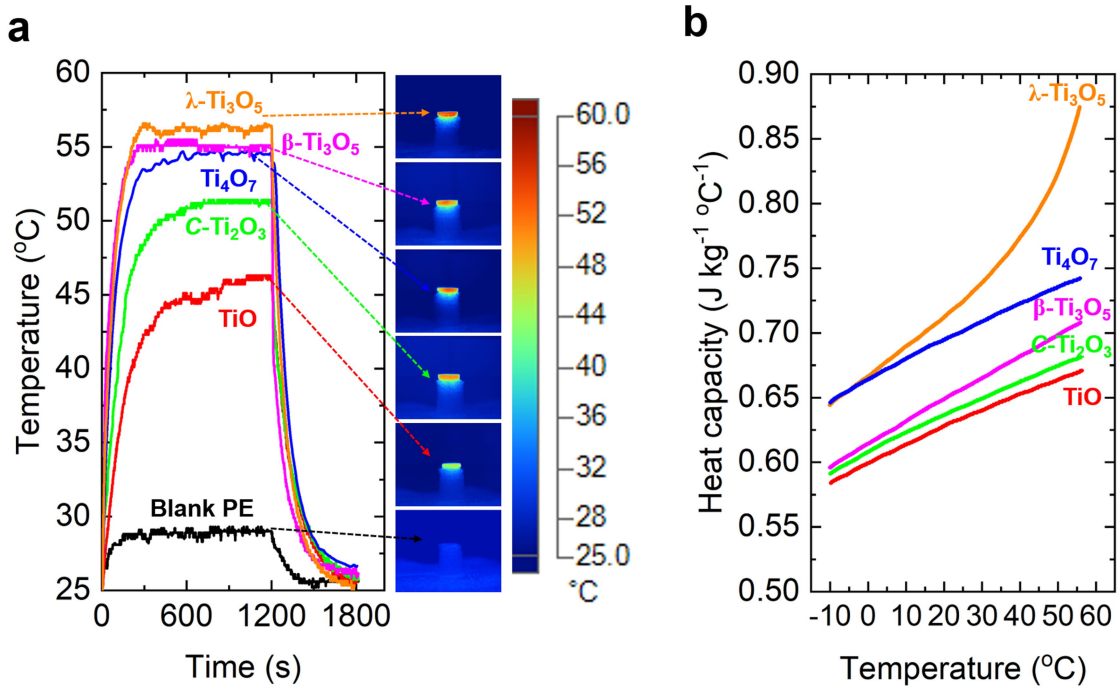

Extended Data Fig. 2 | Surface temperatures and heat capacities of TSOs. **a**, Surface temperature variations of TSO pills (~2 mm in thickness) and blank PE foam (18 mm in thickness) under one sun irradiation (left panel) and infrared photographs taken at the irradiation time of 900 s (right panel). **b**, Specific heat capacities of TSOs at different temperatures. More details are given in Supplementary Information 2.3.

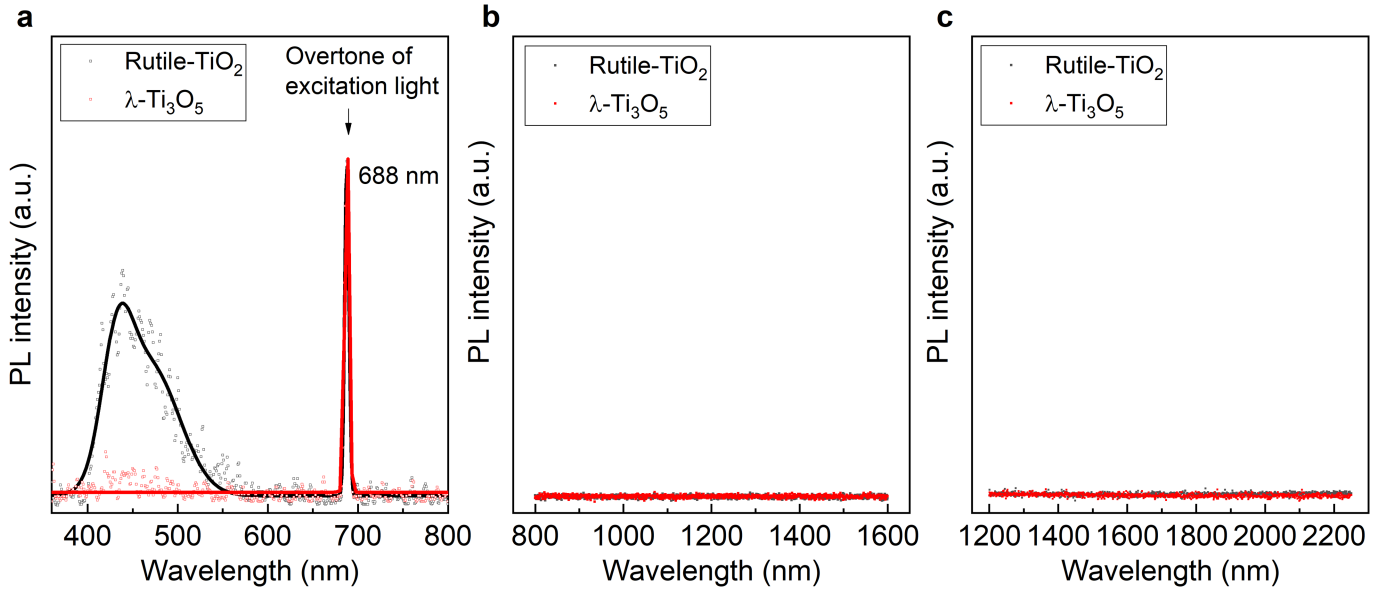

Extended Data Fig. 3 | Experimental photoluminescence (PL) spectra of λ-Ti_3O_5 and rutile-TiO_2 at room temperature (excitation light: 344 nm, emission lights: 360–2250 nm). a, 360–800 nm. **b**, 800–1600 nm. **c**, 1200–2250 nm. More details are given in Supplementary Information 2.4.

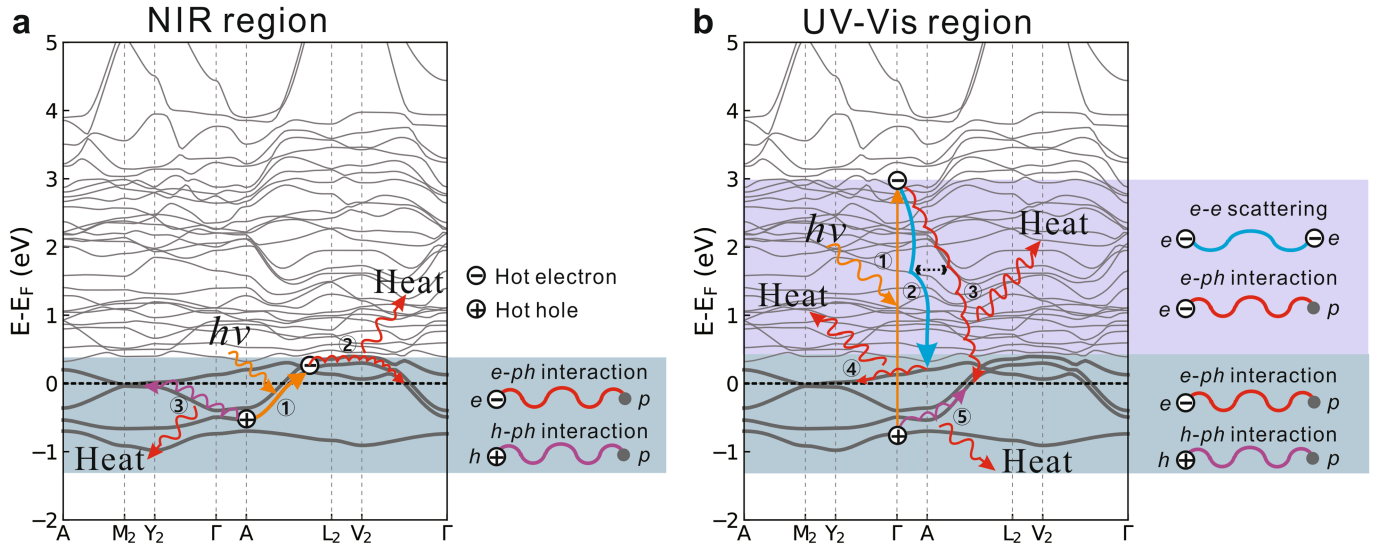

Extended Data Fig. 4 | Schematic of the solar-to-heat conversion in λ-Ti_3O_5. a, Intraband optical transition and electron/hole-phonon (*e-ph*/*h-ph*) interactions in the NIR region. **b**, Interband optical transition, electron-electron (*e-e*) scattering and *e-ph*/*h-ph* interactions in the UV-Vis region. Note that the *e-e* scattering and *e-ph* interactions in **b** may exchange during the relaxation of excited hot electrons, as indicated by dotted line with double arrows. More details are given in Supplementary Information 2.5.

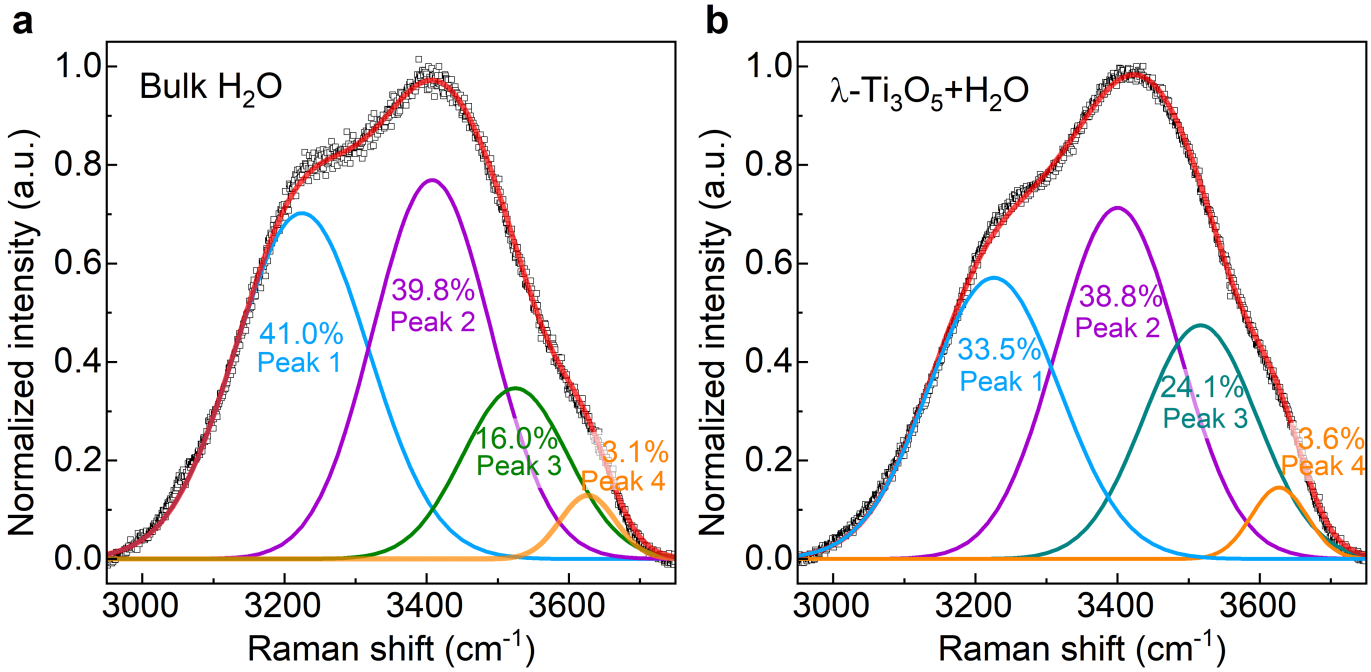

Extended Data Fig. 5 | Raman spectra of bulk water and interfacial water on 2D λ-Ti_3O_5 evaporator in the energy range of O-H stretching modes. a, Bulk water. **b**, interfacial water on 2D λ-Ti_3O_5 evaporator. More details are given in Supplementary Information 4.7.

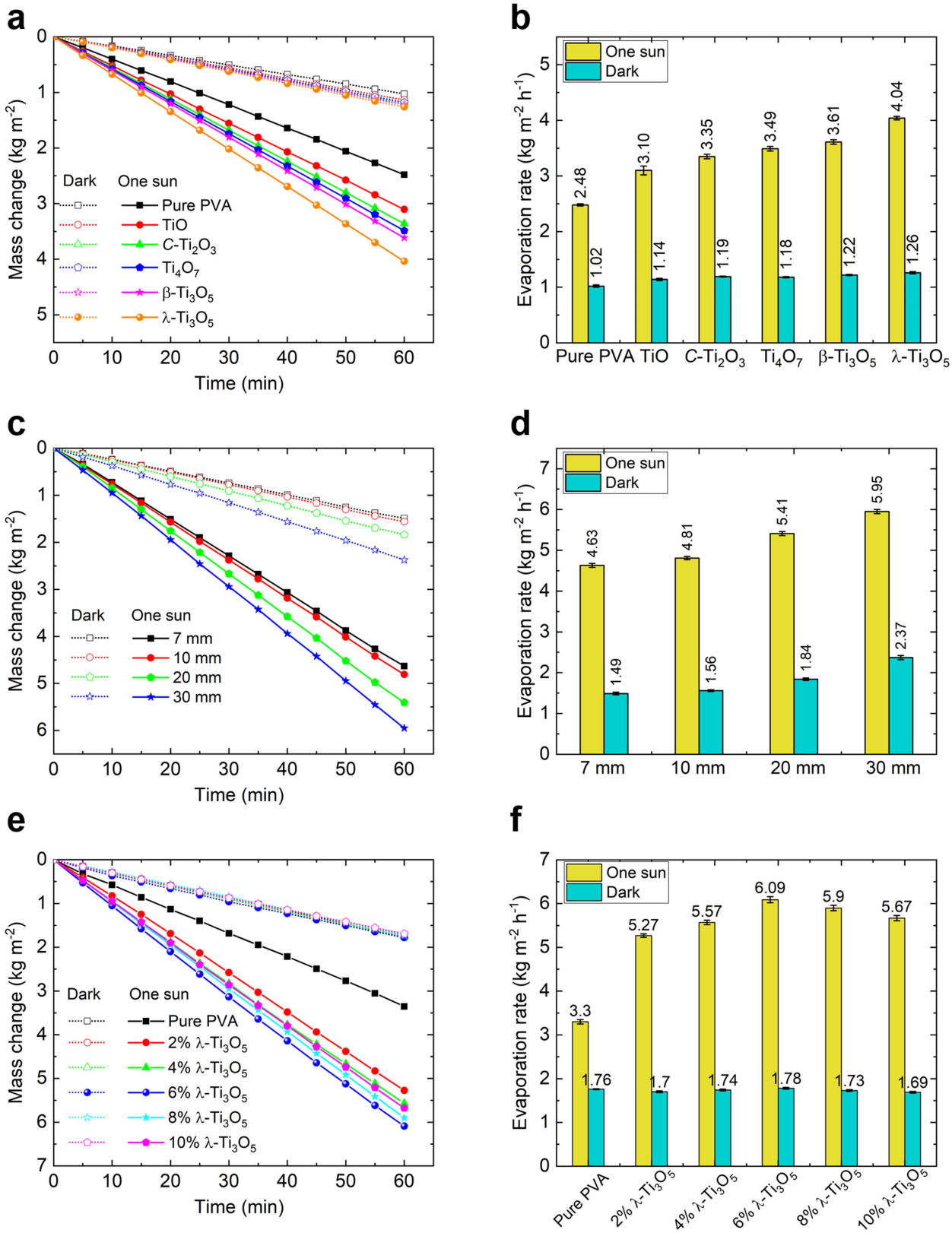

Extended Data Fig. 6 | Water mass changes (left column) and mean measured water evaporation rates (right column) of PVA hydrogel-based 3D-SSEs (15 mm in diameter). a-**b**, 3D-SSEs (7 mm in effective height) with or without an addition of 6 wt% TSO powders. **c**-**d**, 3D-SSEs (6 wt% λ-Ti_3O_5 powders) with different effective height. **e**-**f**, 3D-SSEs (20 mm in effective height) with a conical cavity (14 mm in diameter and 6 mm in depth) and different weight percentage of λ-Ti_3O_5 powders. More details are given in Supplementary Information 5.2. The error bars in **b**, **d**, **f** are the standard deviations of the mean (n = 3, n is the number of evaporation rates for each sample used to derive statistics).

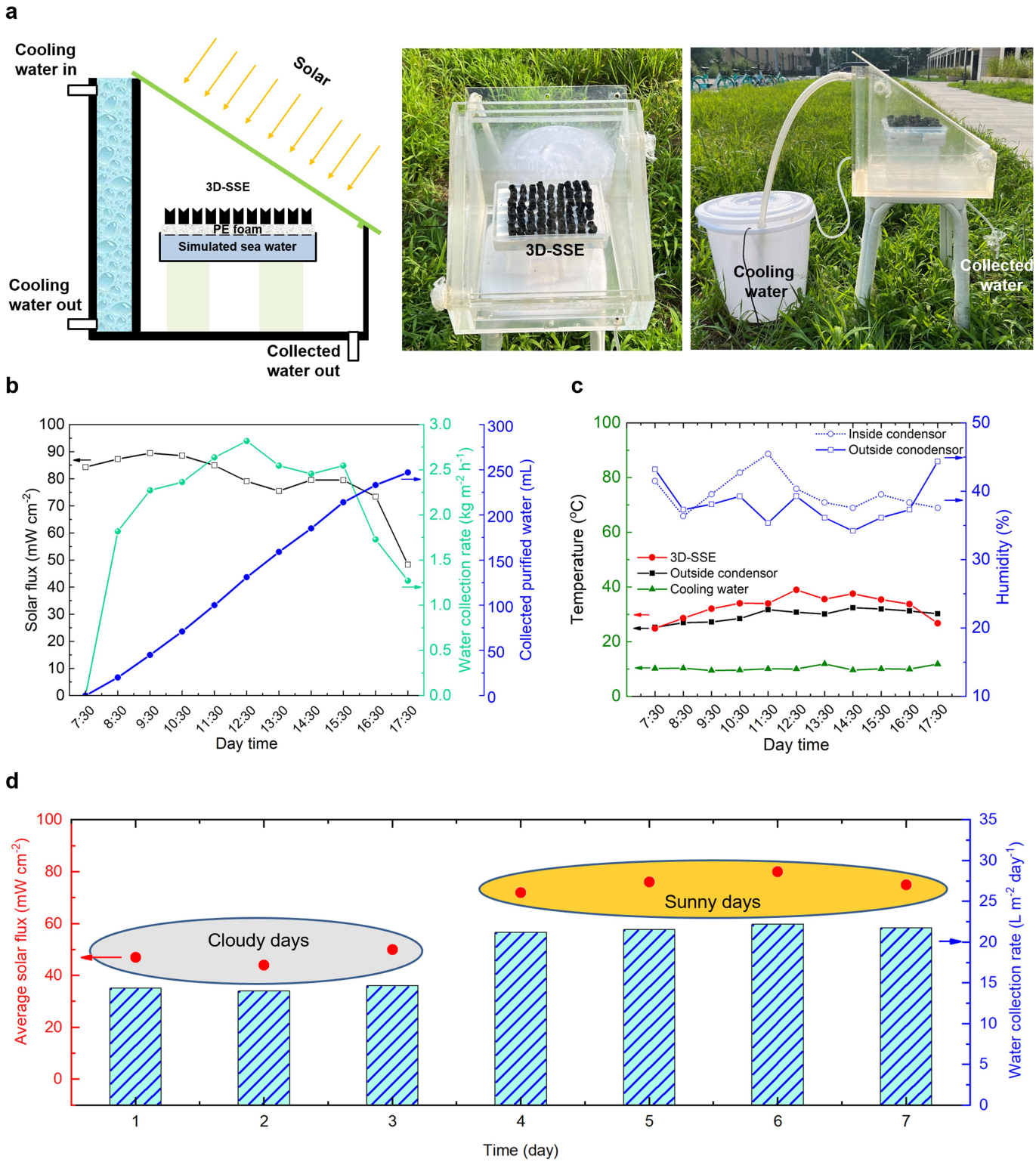

Extended Data Fig. 7 | Outdoor desalination performance of cylindrical 3D-SSEs with a conical cavity under natural sunlight irradiation. **a**, Conceptual design and photographs of the solar water desalination system for salty water purification. **b**, Variations of the solar flux, water collection rate and yield of purified water with day time. **c**, Variations of the temperature and humidity (inside and outside the solar water desalination system) with day time. **d**, Average daily solar fluxes and water collection rates for a duration of 10 h on three cloudy days and four sunny days. More details are given in Supplementary Information 5.5.